Experimental and numerical examination of eddy (Foucault) currents in rotating micro-coils: Generation of heat and its impact on sample temperature

Pedro M. Aguiar, Jacques-François Jacquinot, Dimitris Sakellariou *

Commissariat à l'Énergie Atomique, IRAMIS, Service Interdisciplinaire sur les Systèmes Moléculaires et les Matériaux, F-91191 Gif-sur-Yvette, France

ARTICLE INFO

ABSTRACT

The application of nuclear magnetic resonance (NMR) to systems of limited quantity has stimulated the use of micro-coils (diameter <1 mm). One method recently proposed for the union of micro-coils with Magic Angle sample Spinning (MAS), involves the integration of a tuned micro-coil circuit within standard MAS rotors inductively coupled to the MAS probe coil, termed "magic-angle coil spinning" (MACS). The spinning of conductive materials results in the creation of circulating Foucault (eddy) currents, which generate heat. We report the first data acquired with a 4 mm MACS system and spinning up to 10 kHz. The need to spin faster necessitates improved methods to control heating. We propose an approximate solution to calculate the power losses (heat) from the eddy currents for a solenoidal coil, in order to provide insight into the functional dependencies of Foucault currents. Experimental tests of the dependencies reveal conditions which result in reduced sample heating and negligible temperature distributions over the sample volume.

1. Introduction

There exists significant interest in the application of magnetic resonance methods to samples of ever smaller size. However, the detection of signal from very small numbers of spins is a considerable challenge for NMR. A common method to enhance sensitivity is polarization transfer from abundant spins (e.g., ^{1}H or ^{19}F) via IN-EPT [1] or cross-polarization (CP) [2]. Dynamic nuclear polarization from unpaired electrons [3] is currently witnessing a renaissance in NMR [4]. Cryogenically-cooled probes [5] and alternatives to Faraday induction such as SQUIDs and magnetoresistive sensors (and hybrids thereof) [6–9], force detection [10–12], and optical detection [13,14] also increase detection limits.

It was however, long established that smaller coils generate higher radio-frequency (rf) fields per unit current [15,16]. The *principle of reciprocity* states that the ability of a detector (coil) to detect the precessing magnetic moment **M**, is proportional to its ability to generate rf-fields [17]. Given these two facts, the use of the smallest possible coil for detection of volume-limited samples should yield optimal sensitivity per unit volume. The benefits of micro-coils (diameter <1 mm) were initially demonstrated with ^{1}H

NMR of liquids [18,19]. This has been extended to flow probes, which may be coupled to other analytical techniques such as liquid chromatography, and thanks to their much smaller space requirements, multiple micro-coils have been incorporated into a single probe to increase throughput and/or facilitate suppression of unwanted signals [20–22].

For solid-state NMR, micro-coils were initially applied to wide-line solids under non-spinning conditions [23]. The extremely high radio-frequency (rf) fields generated by these small coils allowed for uniform excitation of very broad spectra, normally difficult to achieve with *typical* coils (4–10 mm in diameter) [24]. The majority of solid-state spectra are, however, acquired under the condition of magic-angle spinning. The compatibility of micro-coils with magic angle spinning is a non-trivial matter; the pursuit to decrease dimensions of current rotor designs to rotor sizes below 1 mm from current materials (e.g., ZrO_2, Si_3N_4) is an engineering challenge. Two alternative methods have recently been devised. Both rely on the use of commercially available equipment, increasing their potential for widespread application. The "piggy-back" design [25] requires modification of an existing MAS probe to allow attachment of a micro-coil, within which is spun a sample inside a micro-capillary. The second method, magic angle coil spinning (MACS) [26], relies on placing a tuned circuit surrounding the sample, inside of a standard rotor and spinning the ensemble. In order to ensure mechanical stability the coil and the sample are placed inside a cylindrical insert that fits tightly inside the rotor. The circuit is inductively coupled to the MAS probe coil and this allows

* Corresponding author. Address: Laboratoire de Structure et Dynamique par Résonance Magnétique, Service Interdisciplinaire sur les Systèmes Moléculaires et les Matériaux, Commissariat à l'Énergie Atomique – Saclay, F-91191, Gif-sur-Yvette, France.

E-mail address: dsakellariou@cea.fr (D. Sakellariou).

for the wireless transmission of current both for excitation and detection.

Friction-induced sample heating under spinning has been observed, and many methods have been established for the measurement/calibration of this heating [27–30]. Under the initial MACS set-up significantly greater heating of the sample, than due to friction, was observed [26]. Much attention – notably pertaining to NMR of biological molecules in high ionic-strength solutions – has recently been given to the issue of radio-frequency induced sample heating [31–33]. Although, the heating observed for MACS arises through a very different mechanism, the magnitude of the heating is at least as large, and thus will present a similar barrier to implementation for such samples. Under MACS, the main source of sample heating arises from the eddy currents created in the conductive materials which experience a temporally-varying magnetic field as they are spun with the rotor inside of the static field, H_0.

In this paper we present work focusing on the calculation of the effect of the geometry on the magnitude of the eddy currents induced in a rotating coil, the heat power they generate and the increased sample temperature. 3D electromagnetic finite elements calculations of the eddy current generation provide numerical solutions to the current distributions in the coil and the power losses. 2D thermal conduction finite elements calculations are employed to convert the theoretically predicted heat to temperatures and allow for comparisons with the experimentally measured ones. These approaches demonstrate qualitative agreement with the predicted geometric dependencies, and provide strategies for future development of optimized MACS inserts.

1.1. Theoretical framework

1.1.1. Generalities

Eddy currents – also called Foucault, after their discoverer – can be generated when relative motion between a conductive material and an external magnetic field exists. The two conditions of a moving conductor/stationary field and moving field/stationary conductor are closely related and may be described by the same set of equations provided that an appropriate reference frame is selected, namely one where the conductor is at rest [34]. This solves the apparent paradox that a conductor rotating in a homogeneous field is subject to eddy currents.

In the presence of a slowly varying magnetic field, $H_{ext} = B_{ext}/\mu_0$ ($\mu_0 = 4\pi\ 10^{-7}\ \mathrm{NA}^{-2}$), Maxwell's equations may be written:

$$\vec{\nabla} \times \vec{E} = -\frac{\partial \vec{B}}{\partial t} \tag{1}$$

$$\vec{\nabla} \cdot \vec{B} = 0 \tag{2}$$

$$\vec{\nabla} \times \vec{H} = \vec{i} \tag{3}$$

where $\vec{E}$ is the induced electric field and $\vec{B}$ the total magnetic induction in the conductor, $\vec{H}$ the total magnetic field and $\vec{i}$ is the (eddy) current density. $\vec{B}$ and $\vec{H}$ include the contributions $\vec{B}_i$ and $\vec{H}_i$ arising from the eddy currents. Since an electric field is created inside a conductor, if there exists a closed path free charges will flow, obeying Ohm's law:

$$\vec{i} = \frac{\vec{E}}{\rho} \tag{4}$$

where ρ is the resistivity. Inside the conductor we assume a constant resistivity, which for an isotropic conductor depends only on the temperature, as well as a constant value of the magnetic permeability, μ, hence:

$$\vec{\nabla} \cdot \vec{H} = \frac{1}{\mu} \vec{\nabla} \cdot \vec{B} = 0 \tag{5}$$

Combining Eqs. (1), (3), (4) and (5) we obtain:

$$\Delta \vec{H} = \frac{\mu}{\rho} \frac{\partial \vec{H}}{\partial t}. \tag{6}$$

In the case of a harmonic variation of the external field all quantities vary as $e^{-j\omega t}$ and we may write:

$$\Delta \vec{H} = -\frac{j\omega\mu}{\rho} \vec{H} \tag{7}$$

This may be simplified in the case where the induced field H_i is small with respect to the external field H_{ext}: the so-called "low-frequency regime". In this case $H \sim H_{ext}$, and since $\Delta H = \Delta H_{ext} + \Delta H_i = \Delta H_i$, we obtain:

$$\Delta \vec{H}_i = -\frac{j\omega\mu}{\rho} \vec{H}_{ext} \tag{8}$$

Eq. (8), may be solved for H_i, under the boundary condition that $H_i = 0$ at infinite distance, and the current density i may be obtained using the following equation:

$$\vec{\nabla} \times \vec{H}_i = \vec{i} \tag{9}$$

Once the current distribution is obtained using Eq. (9), the power losses may be calculated by integration over the volume of the conductor:

$$P = \int_V \rho i^2 d\nu \tag{10}$$

Furthermore, the forces acting on the conductor can also be calculated. They tend to slow the motion of the conductor, an effect commonly used in eddy-current braking. Analytical solutions of Eq. (8) are usually not trivial and have been obtained for only a few model systems [35–37]. Methods for analytical solutions can be found in specialised references [36,37]. The factor $\omega\mu/\rho$, which appears in Eq. (7), is related to the eddy current penetration (skin) depth, which may be calculated using the formula:

$$\delta = \sqrt{\frac{\rho}{\pi\mu\nu}} \tag{11}$$

The low-frequency assumption is valid if δ is large compared to the dimensions of the conductor. For spinning frequencies of 7–35 kHz, we obtain values for δ between 788 and 353 μm for copper coils [$\rho_{Cu}(20\ ^\circ C) = 1.72\ 10^{-8}\ \Omega.m$, and $\mu_{Cu} \cong 1\mu_0$], respectively. This is in accord with the low-frequency regime assumption, since the wires used in MACS are generally of diameter less than 100 μm. This means that the current density due to the eddy current is not present solely on the surface of the wire (as with MHz range radio-frequencies), and indicates that heat losses come from the ensemble of the wire volume, a point of great importance in future designs of MACS coils.

1.1.2. Model systems

Most analytically-solvable systems are two-dimensional or often assumed to have one infinite spatial dimension. The simplest ones include the rotation of a sphere [37], an infinitely long cylinder placed inside a longitudinal or transverse magnetic field [36], and a conducting diamagnetic disk in the presence of either longitudinal or transverse oscillating magnetic fields [35]. Of these three, the thin disk is most relevant for our problem. Thus, we shall begin by considering a diamagnetic, conductive cylindrical disk having a finite thickness in the presence of an *oscillating longitudinal* magnetic field perpendicular to its flat surface (see Fig. 1a). This problem can be exactly-solved analytically providing a benchmark for the software used to solve more complex problems. In this case the eddy currents are confined to circular trajectories inside rings of inner radius, r and outer radius, $r + dr$. If the magnetic field is
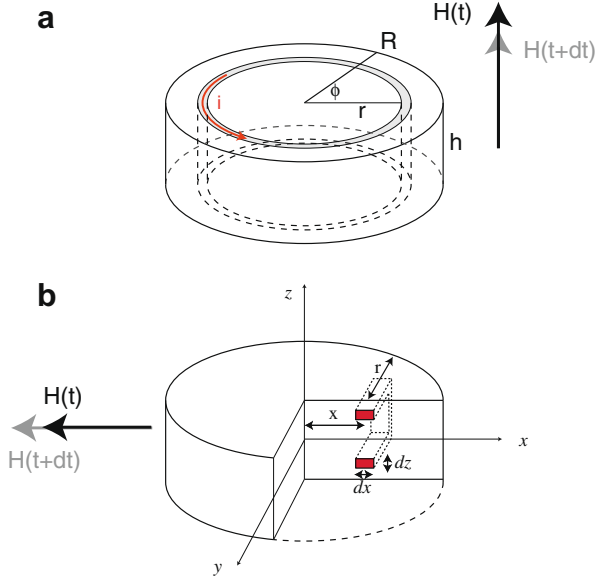
Fig. 1. Cylindrical disk subject to oscillating magnetic fields H(t) perpendicular (a) and transverse (b) to face of the disk. The trajectories of the eddy current paths are shown along with the elementary volumes used for the integration of the power losses.

$\vec{B}(t) = [0, 0, B_0 \cos(\omega_r t)]$, then the electromotive force can be written as $e = -d\Phi/dt = -\pi r^2 B_0 \omega_r \sin(\omega_r t)$, and the resistance of the ring is equal to $R = \rho \frac{2\pi r}{h dr}$. The power dissipation is given by $dP = \frac{e^2}{R}$. Integrating the power over the radius of the disk yields the following:

$$P(t) = \int_0^{D/2} \pi^2 r^4 B_0^2 \omega_r^2 \sin^2(\omega_r t) \frac{h}{2\rho\pi r} dr$$
$$= \frac{\pi}{128} D^4 h \frac{B_0^2 \omega_r^2}{\rho} \sin^2(\omega_r t) \tag{12}$$

The rms power, calculated over one period is:

$$P_{rms} = \frac{\pi}{256} D^4 h \frac{B_0^2 \omega_r^2}{\rho} \tag{13}$$

where B_0 is the magnetic field, ω_r is the angular oscillation frequency, h the thickness of the disk and D its diameter. This result will be compared with numerical simulations in Section 3.1.

We now try to calculate the eddy current losses occurring in a cylindrical diamagnetic conducting disc having a finite thickness in the presence of an *oscillating transverse* magnetic field perpendicular to its flat surface (see Fig. 1b). If we make the approximations that (i) the thickness of the disk is small compared with its diameter and (ii) that the eddy current circulates inside a rectangular frame, then the power losses can be very well approximated [35]. If the magnetic field is $\vec{B}(t) = [B_0 \cos(\omega_r t), 0, 0]$ then the electromotive force can be written as $e = -d\Phi/dt = -4zrB_0\omega_r\sin(\omega_r t)$, and the resistance of the rectangular frame is equal to $R = \rho \frac{4(z+r)}{dxdz}$. The power dissipation on the frame equals $dP = \frac{e^2}{R}$, and this allows us to integrate the power generated over the disk:

$$P(t) = \int 16z^2 r^2 B_0^2 \omega_r^2 \sin^2(\omega_r t) \frac{dxdr}{4\rho(r+z)}$$
$$= 4 \frac{B_0^2 \omega_r^2}{\rho} \sin^2(\omega_r t) \int_0^{h/2} dz \int_0^{D/2} dx \frac{(R^2 - x^2)z^2}{\sqrt{R^2 - x^2 + z}} \tag{14}$$

The approximation that the thickness of the disk is small compared with its diameter can be used to simplify the previous integral to

$\int_0^{h/2} dz \int_0^{D/2} dx \frac{(R^2-x^2)z^2}{\sqrt{R^2-x^2}}$, and allows us to obtain a compact formula for the rms power:

$$P_{rms} = \frac{\pi}{96} h^3 D^2 \frac{B_0^2 \omega_r^2}{\rho} \tag{15}$$

where B_0 is the magnetic field, ω_r is the angular oscillation frequency, h the thickness of the disk and D its diameter. One needs to keep in mind that this formula is not exact, but rather an approximation for a thin disk.

The problem of a *rotating field* is equivalent to the problem of a static conductor in the presence of two orthogonal oscillating magnetic fields having a phase difference of $\pi/2$. The total eddy current density in this case can be written in general as $\vec{i}(t) = \vec{i_1}\cos(\omega_r t) + \vec{i_2}\sin(\omega_r t)$, and the rms power dissipation as the sum of the rms power dissipations from the two orthogonal oscillating fields. Thus, in the case of a static thin disk in the presence of a spinning transverse magnetic field we expect the power losses to be well approximated by:

$$P_{rms} = \frac{\pi}{48} h^3 D^2 \frac{B_0^2 \omega_r^2}{\rho} \tag{16}$$

From all the previous formulas we observe the functional dependence of the eddy current power loss to be proportional to the square of the external magnetic field intensity, proportional to the square of the spinning frequency and inversely proportional to the conductivity of the conductor. The power is also dependent upon the geometric characteristics of the conductor and the orientation of its rotation with respect to the magnetic field.

1.1.3. Eddy currents in MACS

In MACS experiments, the micro-coil is rotated inside the homogeneous magnetic field B_0. The relative motion of the conducting parts of the tuned circuit (coil and capacitor) with respect to the magnetic field will, in general, induce eddy currents. The phenomenon is most readily described by transforming into the rotating frame in which the coil is static and the field is rotated (see Fig. 2). In this frame the component $B_\parallel = B_0 \cos \theta_m$, lying parallel to the axis of the solenoidal coil is static. It has the effect of generating a separation of charges along the interior and exterior surfaces of the coil, and results in no current flow. Thus, we need not consider it any further. The component perpendicular to the coil axis, $B_\perp = B_0 \sin \theta_m$, rotates at the angular frequency ω_r and
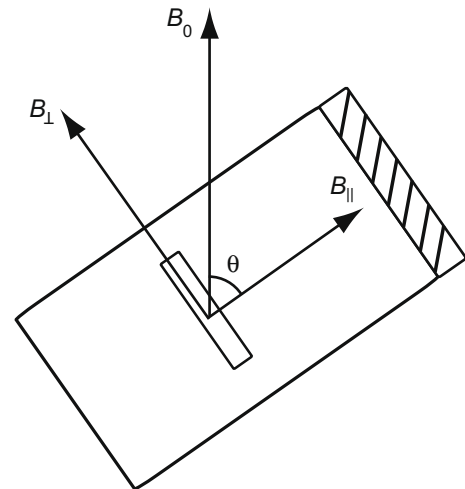

Fig. 2. Orientation of the main magnetic field, B_0 and its longitudinal, $B_\parallel$ and perpendicular, $B_\perp$ components with respect to a single turn of a solenoidal coil. The coil is positioned inside a rotor spinning at the magic angle.

produces eddy currents in the coil due to the flux variations in regions of the wire. The flux going through the coil remains constant, only the flux going through the wire (conductor) changes. To the best of our knowledge it is not possible to derive an analytical expression for the geometric dependence even when the coil is made of a single turn [37]. In what follows we will consider a simple model of a single turn ring, having a rectangular cross section, height h, width w and of radius r (see Fig. 3). We then make a number of assumptions in order to obtain some qualitative formulas.

In the case of a field, $B_\perp$ rotating about a conductor, eddy currents will be induced such that the current flow in each elementary loop is creating a field opposing the variation of the flux in that loop. One can distinguish two current trajectories (see Fig. 3). The first are roughly elliptical trajectories of axis perpendicular to $B_\perp$ and the cross section of the wire. The second are roughly circular trajectories of axis perpendicular to $B_\perp$ and approximately parallel to the cross section of the wire. Such circulating currents generate a small magnetic field, which will be inhomogeneous over the sample volume. The characteristics of this field: magnitude and homogeneity, are currently being investigated and will not be the focus of this paper.

For the elliptical trajectories one can consider an "average" trajectory whose longitudinal and transverse dimensions are of the order of r and h, respectively, and which is crossed by a flux,

$$\phi = B_\perp rh \sin(\omega_r t) \tag{17}$$

in the rotating field frame. The electromotive force can be calculated from the flux formula at $t = 0$, and is given by:

$$e = -\frac{d\phi}{dt}_{(t=0)} = -\omega_r B_\perp rh \tag{18}$$

The effective resistance for the average trajectory is,

$$R = \frac{\rho l}{S} \tag{19}$$

where S is half the cross-sectional area of the wire ($S = wh/2$) and l ($l \sim 2r$) defines the total length of the trajectory. The Joule dissipation in this sector of the coil is thus given by:

$$P = \frac{e^2}{R} \approx \omega_r^2 B_\perp^2 r^2 h^2 \left(\frac{wh}{4\rho r}\right) = \omega_r^2 B_\perp^2 \left(\frac{rh^3 w}{4\rho}\right) \tag{20}$$
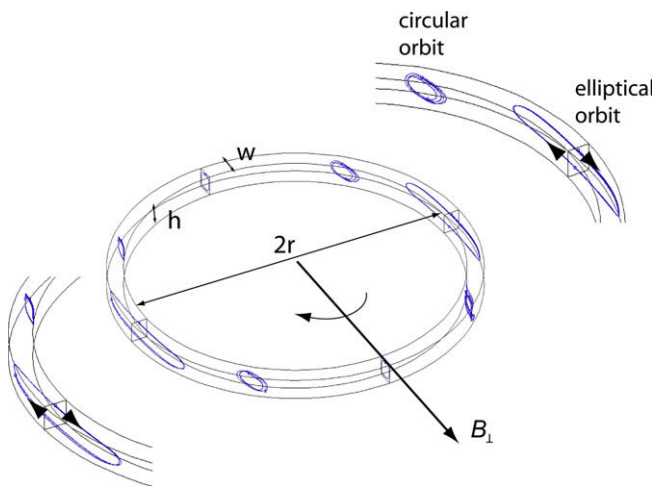

Fig. 3. Calculated trajectories of the generated Foucault currents for a single loop (turn). Two distinct trajectories (and regions) are observed throughout the loop. The width, w, height, h and radius, r of the loop, $B_\perp$ as well its sense of rotation are noted. To the top right is an expansion showing more clearly the circular and elliptical orbits of the eddy currents, along with the direction of current flow.

For the circular trajectories, the previous approximations are even cruder, but simulations confirm that a similar value of the dissipation should be expected. Over the 4 sectors of the coil we thus find:

$$P \approx 4 * \omega_r^2 B_\perp^2 \left(\frac{rh^3 w}{4\rho}\right) = \omega_r^2 B_\perp^2 \left(\frac{rh^3 w}{\rho}\right) \tag{21}$$

This formula provides merely an approximation to P. In what follows, we perform numerical simulations in order to check the validity and precision of this model.

2. Materials and methods

2.1. Electromagnetic calculations

3D electromagnetic calculations of the induced Foucault currents were performed on a Pentium IV desktop computer, using the Flux3D version 10.1.2 (Cedrat) software package [38]. All models were calculated using copper as the conductor ($\rho_{20\,°C} = 1.72\ 10^{-8}\Omega m$). For the model of a thin disk the parameters were set to: $H_{rms} = 1,000,000$ A/m, $D = 11.0$ mm, $h = 1$ mm and $h = 0.1$ mm, and $\omega_r/2\pi = 10$ Hz. For the problem of MACS, we calculated the effects of the rotating magnetic field on a model consisting of a single turn of rectangular cross-section placed inside an *infinite* volume occupied by air. The boundary conditions were set automatically by the software (magnetic potential null at infinite distance) and the presence of a homogeneous rotating magnetic field was explicitly included as two oscillating magnetic fields of equal magnitude in quadrature. Appropriate mesh density was determined by testing for convergence of the results upon decreasing mesh size. The number of nodes in the mesh was of the order of 50,000–200,000 depending on model dimensions. All files are accessible upon request to the authors. Calculations to test functional dependencies were performed manually: varying the independent geometric parameters in order to establish their impact on the eddy currents.

2.2. Thermal calculations

Calculations of the heat conduction were carried-out on a Pentium IV desktop computer, using the Quickfield software package (version 5.0.3.41, Terra-Analysis). A model including the coil, quartz capillary (thermal conductivity, $k = 1.4$ W/Km), heat transfer paste ($k = 1.7$ W/Km), Shapal-M ($k = 80$ W/Km) or Kel-F ($k = 0.21$ W/Km) insert, and the zirconia ($k = 2.4$ W/Km) rotor was employed. The coil was simulated as a single "cylindrical" infinitely-thin heat source with a length of 0.8 mm (comparable to the measured lengths of the coils). A constant temperature at the outer-wall of the system (rotor) was imposed as a boundary condition, which seemed reasonable given the very-rapid air-flow (bearing, and variable-temperature gas) which pass over the outer surface of the rotor under typical MAS conditions.

2.3. Lead-207 NMR

[207]Pb spectra were acquired at 104.056 MHz using a Bruker Avance II 500 spectrometer equipped with a widebore 11.7 T magnet, and 4 mm double- or triple-resonance MAS probes with temperature control, used to maintain constant the temperature of the gas entering the probe. Chemical shifts were converted to temperatures using the well-established temperature dependence of lead nitrate of 0.758 ppmK^{-1} [28,39,40]. Hand-wound coils were made using either 25, 62 or 80 µm diameter insulated copper wire, consisting of 5 turns, and lengths of *ca.* 0.7–0.9 mm. The coils were affixed to fused quartz capillaries (Vitrocom CV5070) of outer

diameter 0.7 mm and inner diameter of 0.5 mm, with a minimum of a fast-drying cyanoacrylate glue. Dry potassium bromide (dried overnight at ~110 °C) was packed into the bottom of the capillaries (previously flame-sealed at one end) just up to the bottom end of the coil. Lead nitrate was added to the capillary to completely fill the coil volume. The sample was packed as tightly as possible in a fashion similar to traditional MAS rotors using a cylindrical "packing tool" of dimensions commensurate with the length and inner diameter (ca. 13 mm and 0.4–0.5 mm, respectively) of the capillary. Cylindrical inserts with inner diameters of 0.9 mm, and outer diameters machined to fit snugly inside of a standard Bruker 4 mm rotor were used in order to centre the capillary in the rotor. Experiments with untuned coils were performed with both aluminum nitride (Shapal-M) and chlorotrifluoropolyethylene (Kel-F) inserts.

Experiments on a tuned coil were made using the same 0.7 mm (o.d.) capillaries (packed in the same fashion) with a coil made from 25 μm wire, consisting of 18 turns (~1.6 mm length) and tuned to ~103.5 MHz, with a quality factor, Q ~50 using a 22 pF chip capacitor (Murata manufacturing Co. Ltd.) having dimensions of 0.4 mm × 0.2 mm × 0.2 mm. The capillary/coil was placed inside of a ceramic Shapal-M insert.

3. Results and discussion

3.1. Foucault current calculations

Benchmark testing of the software on a model containing a disk in the presence of an oscillating longitudinal and transverse field was performed. In the case of a longitudinal field the agreement of the simulated power losses with Eq. (13) was excellent (0.1251498 versus 0.1251517 W, respectively). In the case of a transverse oscillating magnetic field the simulated values were very close to the ones from Eq. (15). A deviation of ~1% was observed (2.7407 mW numerically versus 2.75817 mW analytically) as long as the height was at least 20 times smaller than the

diameter. Outside this "thin disk" approximation one could take into account the losses along the z-axis (Fig. 1b), which were originally neglected. Doing so results in an improved agreement with the numerical result. Notice, however, that the assumption that the current is confined inside a rectangular frame with uniform thickness is by no means obvious and can justify these small discrepancies. In fact, we observe that the current paths for disks of finite thickness display some degree of curvature (which decreases as the thickness of the disk is reduced).

For the MACS simplified numerical model, the geometric parameters were manually varied and the power dissipation was monitored as a function of spinning frequency, magnetic field amplitude, width, height and diameter of the coil (see Fig. 4). The field and rotation frequency were both found to conform to the expected square power dependence. The numerical results for a single-turn ring lead to slightly different power exponents for the radius, the height and the width of wire, than those of Eq. (21). In addition we find a systematic overestimation of the heat power losses using Eq. (21). This means that the approximations made in the derivation of Eq. (21) are not rigorous. A fit of the numerical results leads to the following formula for the losses:

$$P = k\omega_r^2 B_\perp^2 \frac{r^{0.92}}{\rho} \left(\frac{\sqrt{\pi}a}{2}\right)^{4.08} \tag{22}$$

where, $k = 0.5$.

In the case of wire with a circular cross-section of radius $a/2$, we can derive a variant of Eq. (22), using the radius in place of the height and width, under the assumption of identical power losses for constant cross-sectional area, which yields the following:

$$P = kn\omega_r^2 B_\perp^2 \frac{r^{0.92}}{\rho} \left(\frac{\sqrt{\pi}a}{2}\right)^{4.08} \tag{23}$$

For an n turn solenoidal coil, the unitary dissipation should be multiplied by the number of turns, n giving:
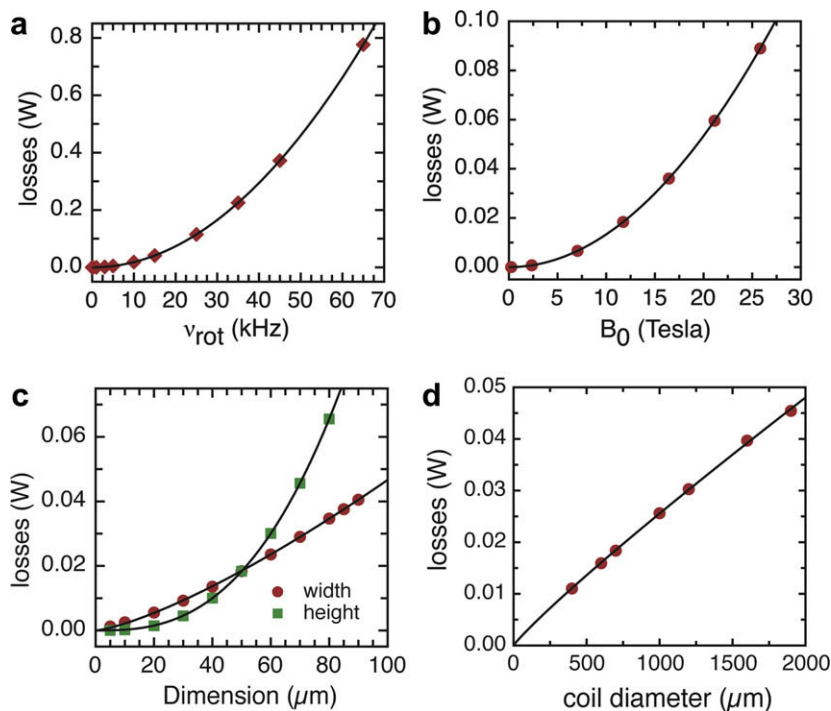

Fig. 4. Results of numerical simulations for the dependence of the eddy current power losses on (a) rotation frequency, (b) magnetic field, (c) wire dimensions (width and height) and (d) the diameter of the coil. The solid lines represent the best-fit curves and were used to extract the power components of Eq. (22). The sum of the power exponents for the width, height and diameter was fixed to 5, as required by dimensional analysis.

$$P = kn\omega_r^2 B_\perp^2 \left(\frac{2r^{0.91}a^{4.08}}{\rho\sqrt{\pi}} \right) \qquad (24)$$

Notice that the value of k is not necessarily the same for round wire as for rectangular cross section wire and can only be calculated by numerical simulation.

3.2. ^{207}Pb NMR thermometry

The observed sample temperature is a function of two processes: (i) The heat generated by the circulating eddy currents in the coil and (ii) the efficiency of heat dissipation from the coil to the outer surface of the rotor. First, experiments with Kel-F inserts were employed in order to minimize the latter effect to the observed temperature, thus minimizing the effects of "minor" imperfections in the contact at the various interfaces, which can significantly impact the temperature observed at the sample (*vide infra*). Experiments with the 80 μm diameter wire were found to result in heating of the sample by ~81 °C at 6 kHz spinning, in addition to frictional heating, whereas the 62 and 25 μm wire yielded 36.9 and 2.4 degrees, respectively, at the same spinning rate. An experiment with the same sample, capillary and insert at the same spinning frequency but without any microcoil was performed in order to determine the frictional heating contribution to the temperature. The temperature results show a power dependence on the radius of ~3.1 (see Fig. 5), rather than the expected fourth-power dependence of the eddy current power losses.

Experiments performed using the Shapal-M insert exhibited reduced heating relative to that observed with Kel-F inserts at the same spinning rate, because of the higher thermal conductivity of Shapal-M (~80 W/Km) than Kel-F (~0.21 W/Km). In fact, experiments carried out with Shapal-M at 15 kHz yielded similar heating to Kel-F at 6 kHz (see Fig. 5). However, the power dependence of the temperature on the wire diameter deviated from Eq. (24) by a greater amount (power of ~2.5).

The total heating with 80 μm wire resulted in a sample temperature of over 99 °C at only 12 kHz spinning! As with the initial tests on 7 mm MACS setup, the addition of a commercial heat transfer compound (HTC—Electrolube HTC35SL) to the outer side of the coil resulted in a significant reduction of the sample temperature. This is due to the enhanced heat transfer away from the sample. In this case for 80 μm wire and 12 kHz spinning the addition of HTC resulted in a lowering of the sample temperature to 55 °C, and a sample temperature of only 86 °C at 15 kHz spinning frequency. As expected the 25 μm wire resulted in the smallest measured temperature increase. In fact, it exhibited slightly lower (2–6°) temperatures than a full 4 mm rotor. Measurement of the frictional heating for an identical capillary without coil, was found to yield even lower heating (4–15° over the range of spinning rates from 4 to 15 kHz).

The untuned coils allowed for isolation of heating arising from the coil (as opposed to that from the leads and capacitor). However, the low signal-to-noise impedes the acquisition of multiple spectra in a timely manner. This hinders the testing of the spinning rate dependence of the heat power. When untuned micro-coils were used, the NMR signal is detected by the 4 mm probe coil. The use of tuned micro-coil provides a much higher signal sensitivity allowing for much faster acquisition of spectra, and thus a more detailed look at the spinning frequency dependence of the heating. In addition, the use of an 18 turn coil (whose increased inductance was necessary in order to tune to such a low frequency) provides larger temperature increases than the 5 turn untuned coils. The observed heating of the sample (with respect to the non-spinning condition) for both the micro-coil and a standard 4 mm rotor, in the same MAS probe are shown in Fig. 6. The temperature dependence on the rotation frequencies in both cases is reasonably well

described assuming a standard ω_r^2 dependence (solid black lines, Fig. 6). The increased temperatures with this tuned coil in comparison to the untuned one are inline with a linear dependence on the number of turns. This indicates that only a small contribution to the overall sample heating for a 18 turn coil arises from the capacitor and the coil leads.

In addition to the maximum temperature of the sample another property of interest is the spatial distribution of temperatures. Temperature gradients for standard rotors are well-known [41]. We observe similar results with our standard 4 mm rotor, for which at 15 kHz spinning we measure a temperature distribution of 14 °C (as measured by the peak width at 20% height). We find (see Fig. 7) that this distribution of temperature increases with the diameter of wire. At 15 kHz spinning the distributions are 2.4°, 2.5°, 34.5° and 50.7° for capillaries with no coil, 25, 62 and 80 μm wire, respectively. The tuned micro-coil was found to have temperature distributions of ~2° over the spinning frequency range of 3–10 kHz. This is a rather interesting benefit of the much smaller wire diameter, and may be even more important than the simple reduction of the overall heating upon moving to the much narrower wires, since a uniform correction to the temperature may be obtained by the application of cooled air to the system. However, such cooling would be highly unlikely to significantly
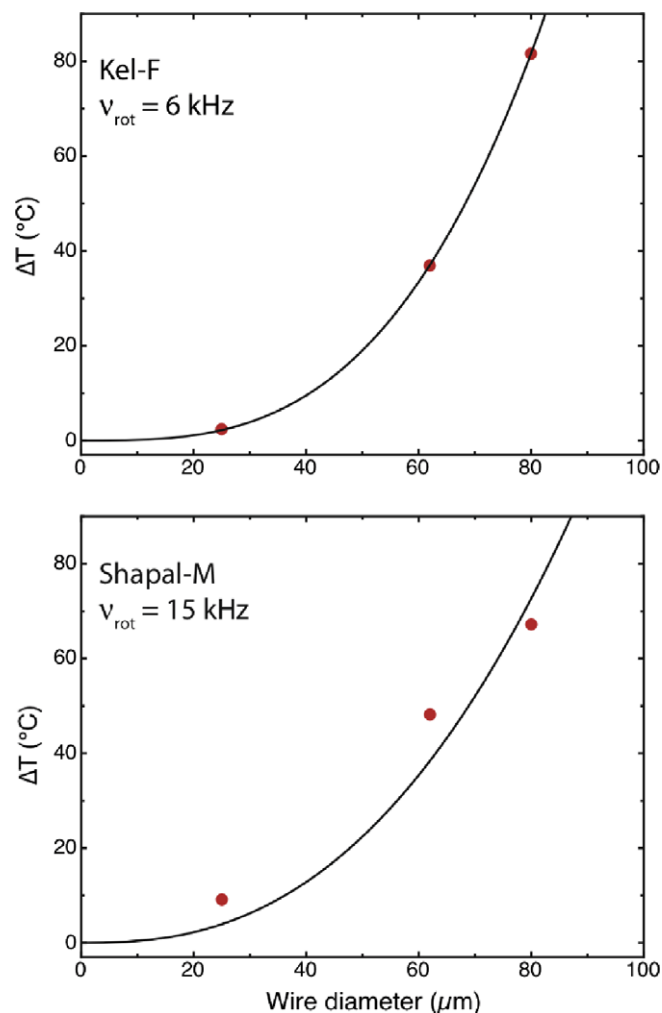

Fig. 5. Observed change in temperatures (relative to capillary with no coil) for a coil of given wire diameter under 6 kHz spinning with Kel-F insert and 15 kHz spinning with Shapal-M insert. The fit to the data for the Kel-F insert is closer to the theoretical 4 (3.1), whereas with Shapal-M the dependence is roughly to the power of 2.5 (Note that no temperature corrections were included in the resistivity).
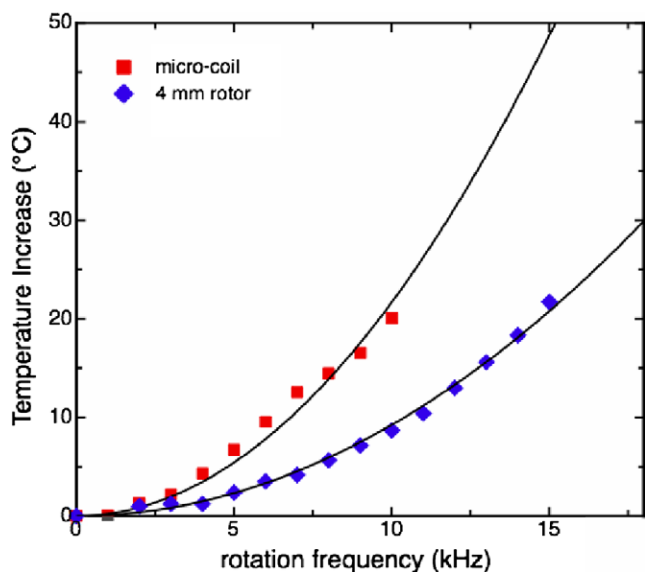
Fig. 6. The heating observed for a standard 4 mm rotor (blue diamonds) and a tuned microcoil consisting of 18 turns of 25 μm wire, 0.7 mm i.d. and length of 1.6 mm in a Shapal-M insert (red squares). Best-fits to a square dependence of the temperature with rotation frequency for each is also shown (solid black lines).
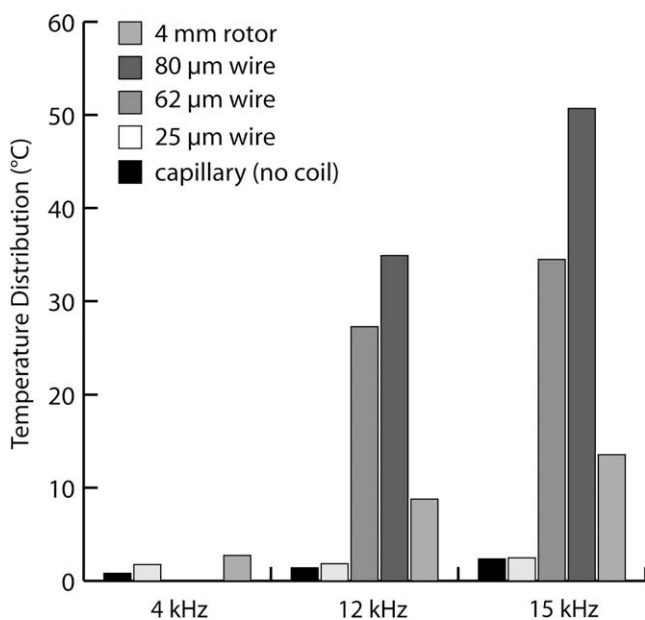

Fig. 7. The temperature distributions present throughout the sample volume as determined from the linewidth of the ^{207}Pb resonance at 20% of the peak maximum at the noted spinning rates, for a capillary with no coil, 25 μm wire coil, 62 μm, 80 μm and a full 4 mm rotor (all coils were untuned).

impact the temperature distribution. This can be important for both HRMAS experiments using MACS as many small molecules

have temperature dependent shifts (e.g., water, ethylene glycol, methanol etc.), as well as for rigid solids which are temperature dependent such as paramagnetic solids, or many heavy metals and/or for studying dynamics, where the use of a coil which imparts a distribution of temperatures of 30–50 degrees would hinder accurate rate measurements.

3.3. Heat-transfer efficiency

In an attempt to convert the theoretical heat power into a temperature we performed numerical simulations of the heat-transfer. Using Eq. (24) we can estimate the heat power generated by the three (25, 62 and 80 μm wire diameter) untuned solenoids at the various spinning rates for which we have experimental data. Using these heat powers and assuming perfect contact with the Kel-F insert we slightly overestimate – by roughly 20% – the experimental sample temperatures (select values given in Table 1), but reasonable correlation between the two is obtained (R^2 = 0.981). This may arise because of the approximations in going from a model with rectangular cross-sectional area to one of circular cross section.

For the case of the Shapal-M insert the deviation of the predicted sample temperatures from those observed experimentally, are significantly greater than those observed with the Kel-F insert (see Table 1). Inspection of the calculated temperature distributions for the Kel-F and Shapal-M inserts (Fig. 8c and d) show poor thermal conduction outward from the coil for the former case. In the latter, the heat is, more efficiently transferred away from the heat source (i.e., the coil) to the outer edge of the insert. Thus, the Shapal-M is more susceptible to minor imperfections in contact at any of the interfaces; coil-capillary; coil-HTC paste; coil-insert; insert-rotor.

Calculations of models taking into account the discrete nature of the coils (i.e., as a series of loops rather than a single uniform surface) provided no improvement in the correlation with the experimental results, for either the Kel-F or Shapal-M insert models. It was found that temperatures closer to experiment could be obtained using models including "air-gaps". The two most reasonable places fro such gaps were between the coil (heater) and insert, and between the insert and rotor wall. The insertion of air-gaps (thermal conductivity ~0.02 W/Km) of 10–50 μm yielded improved correlation of the temperatures with those measured for both insert materials.

3.4. Strategies for optimum temperature control

The use of even smaller wire diameters is hampered by the difficulties involved in their handling. However, recent 3D lithographic processes for fabricating micro-coils could allow for further significant reductions in wire size [42,43]. The precision in geometry obtained by such fabrication methods should also allow for further optimization of all independent geometric parameters vis-à-vis Eq. (22). One potential issue with such coils is their generally poorer quality factors.

We have demonstrated that achieving good contact is key to ensuring the efficient transfer of heat away from the sample. The

Table 1
Calculated heat power generated, predicated and experimental sample temperatures for the untuned coils with Kel-F (6 kHz) and Shapal-M (15 kHz) inserts.

Wire o.d. (μm)	Kel-F ν_{rot} = 6 kHz			Shapal-M, ν_{rot} = 15 kHz		
	P (mW)[a]	T_{pred}(°C)	T_{exp}(°C)	P (mW)[a]	T_{pred}(°C)	T_{exp}(°C)
25	1.1	1.2	1.6	6.0	0.11	9
62	45	45	37	209	3.7	48
80	113	111	81	560	9.8	67

[a] The resistivity is corrected for the actual sample temperature measured using: $\rho(T) = 0.0039(T-20)\rho(20°C) + \rho(20°C)$, where $\rho(20°C) = 1.72 \times 10^{-8}\Omega m$.
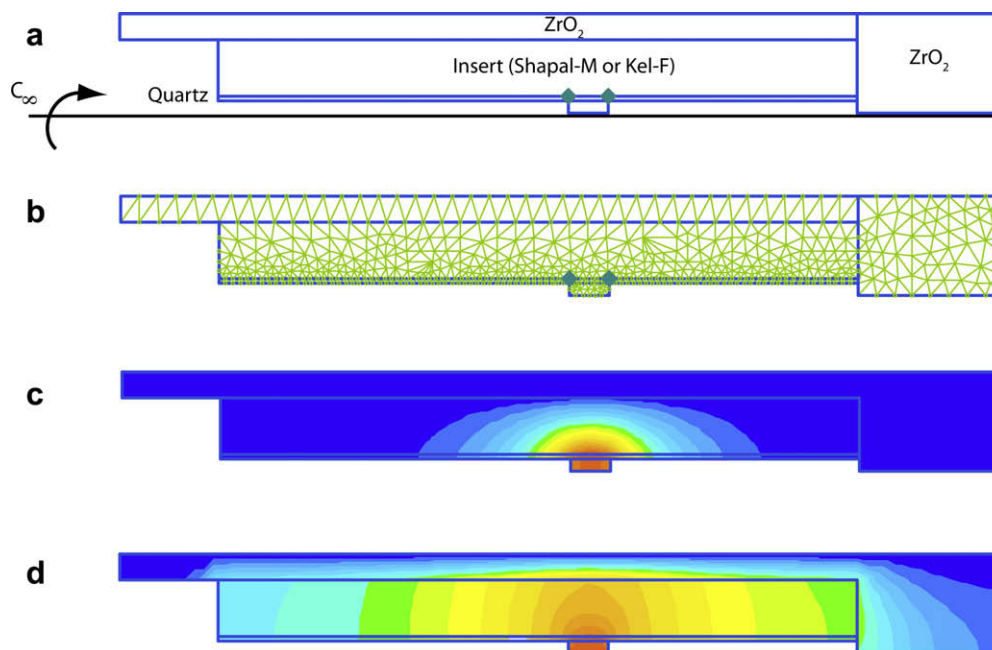
Fig. 8. Model used for thermal simulations, (a) showing the overall layout and symmetry, (b) the mesh employed (~31 nodes/mm^2), (c and d) example results with Kel-F and Shapal-M inserts, respectively. Note that the scales for (c and d) are not identical, having maxima of 91 and 1.7 °C, respectively. In the case of Kel-F the lower thermal conductivity minimizes the impact of imperfections in contact between the various components (coil, insert, and rotor) on the sample temperature. The much greater thermal conductivity of Shapal-M makes these contacts more important for efficient heat transport.

greater regularity of such lithographic coils should also allow for better contact of the coil with the insert material and thus more efficient heat evacuation. Although technically challenging, the use of such techniques to deposit the coil directly onto the inner-side of the insert should provide the best contact and based on our numerical calculations of heat-transfer negligible sample heating.

4. Conclusions

A theoretical examination of the eddy currents and their heat power dissipation was presented. Numerical simulations were used to ascertain their geometric dependencies. The results obtained with Kel-F inserts yielded observed temperatures in close agreement with those predicted from our formulated theoretical framework. Experiments with Shapal-M inserts yielded significantly reduced heating. However, our predictions in this case are not in accordance with experiments, which can be partially explained by imperfect contact at all interfaces, resulting in inefficiencies in the heat transfer from the coil to the outer-wall of the rotor. Despite this, a significant reduction in the sample heating was found to be achievable with the use of 25 μm diameter wire, which is commercially available and strong enough to be wound without breakage. The distribution of temperatures for the MACS setup using the 25 μm wire was found to be almost negligible and in fact much narrower than that for standard 4 mm rotors. The experiments with the tuned micro-coil represent the first MACS experiments on 4 mm rotors and the conclusions from this study could benefit future improved designs of MACS inserts.

References

[1] G.A. Morris, R. Freeman, Enhancement of nuclear magnetic resonance signals by polarization transfer, Journal of the American Chemical Society 101 (1979) 760–762.
[2] A. Pines, M.G. Gibby, J.S. Waugh, Proton-enhanced nuclear induction spectroscopy. Method for high-resolution NMR of dilute spins in solids, Journal of Chemical Physics 56 (1972) 1776–1777.
[3] A. Abragam, M. Goldman, Principles of dynamic nuclear polarisation, Reports on Progress in Physics (1978) 395.
[4] T. Maly, G.T. Debelouchina, V.S. Bajaj, K.N. Hu, C.G. Joo, M.L. Mak-Jurkauskas, J.R. Sirigiri, P.C.A. van der Wel, J. Herzfeld, R.J. Temkin, R.G. Griffin, Dynamic nuclear polarization at high magnetic fields, Journal of Chemical Physics 128 (2008) 052211–052219.
[5] G.E. Martin, Cryogenic NMR probes: applications, in: D.M. Grant, R.K. Harris (Eds.), Encyclopedia of Nuclear Magnetic Resonance, Wiley, New York, 2002.
[6] Y.S. Greenberg, Application of superconducting quantum interference devices to nuclear magnetic resonance, Reviews of Modern Physics 70 (1998) 175.
[7] F. Verpillat, M.P. Ledbetter, S. Xu, D.J. Michalak, C. Hilty, L.S. Bouchard, S. Antonijevic, D. Budker, A. Pines, Remote detection of nuclear magnetic resonance with an anisotropic magnetoresistive sensor, Proceedings of the National Academy of Sciences of the United States of America 105 (2008) 2271–2273.
[8] M. Pannetier-Lecoeur, C. Fermon, N. Biziere, J. Scola, A.L. Watlliang, RF response of superconducting-GMR mixed sensors, application to NQR, IEEE-Inst Electrical Electronics Engineers Inc. (2007) 598–601.
[9] M. Pannetier, C. Fermon, G. Le Goff, J. Simola, E. Kerr, Femtotesla magnetic field measurement with magnetoresistive sensors, Science 304 (2004) 1648–1650.
[10] J.A. Sidles, D. Rugar, Signal-to-noise ratios in inductive and mechanical detection of magnetic resonance, Physical Review Letters 70 (1993) 3506.
[11] J.A. Sidles, Noninductive detection of single-proton magnetic resonance, Applied Physics Letters 58 (1991) 2854.
[12] L.A. Madsen, G.M. Leskowitz, D.P. Weitekamp, Observation of force-detected nuclear magnetic resonance in a homogeneous field, Proceedings of The National Academy of Sciences 101 (2004) 12804–12808.
[13] J. Manuel, C. Cohen-Tannoudji, Spectroscopie Hertzienne—Detection Optique De La Resonance Magnetique Par Modulation De L'effet Faraday Paramagnetique Transversal A La Frequence De Larmor, Comptes Rendus Hebdomadaires Des Seances De L Academie Des Sciences 257 (1963) 413.
[14] I.M. Savukov, S.-K. Lee, M.V. Romalis, Optical detection of liquid-state NMR, Nature 442 (2006) 1021–1024.
[15] C.-N. Chen, D.I. Hoult, Biomedical Magnetic Resonance Technology, Adam Hilger, 1989.

[16] D.I. Hoult, NMR receiver—description and analysis of design, Progress In Nuclear Magnetic Resonance Spectroscopy 12 (1978) 41–77.

[17] D.I. Hoult, The principle of reciprocity in signal strength calculations—a mathematical guide, Concepts In Magnetic Resonance 12 (2000) 173–187.

[18] D.L. Olson, T.L. Peck, A.G. Webb, R.L. Magin, J.V. Sweedler, High-resolution microcoil H-1 NMR for mass-limited, nanoliter-volume samples, Science 270 (1995) 1967–1970.

[19] N.A. Wu, T.L. Peck, A.G. Webb, R.L. Magin, J.V. Sweedler, H-1 NMR spectroscopy on the nanoliter scale for static and online measurements, Analytical Chemistry 66 (1994) 3849–3857.

[20] M.A. Macnaughtan, T. Hou, E. MacNamara, R.E. Santini, D. Raftery, NMR difference probe: a dual-coil probe for NMR difference spectroscopy, Journal of Magnetic Resonance 156 (2002) 97–103.

[21] T. Hou, J. Smith, E. MacNamara, M. Macnaughtan, D. Raftery, Analysis of multiple samples using multiplex sample NMR: selective excitation and chemical shift imaging approaches, Analytical Chemistry 73 (2001) 2541–2546.

[22] G. Fisher, C. Petucci, E. MacNamara, D. Raftery, NMR probe for the simultaneous acquisition of multiple samples, Journal of Magnetic Resonance 138 (1999) 160–163.

[23] K. Yamauchi, J.W.G. Janssen, A.P.M. Kentgens, Implementing solenoid microcoils for wide-line solid-state NMR, Journal of Magnetic Resonance 167 (2004) 87–96.

[24] J.A. Tang, L.A. O'Dell, P.M. Aguiar, B.E.G. Lucier, D. Sakellariou, R.W. Schurko, Application of static microcoils and WURST pulses for solid-state ultra-wideline NMR spectroscopy of quadrupolar nuclei, Chemical Physics Letters 466 (2008) 227–234.

[25] H. Janssen, A. Brinkmann, E.R.H. van Eck, P.J.M. van Bentum, A.P.M. Kentgens, Microcoil high-resolution magic angle spinning NMR spectroscopy, Journal of the American Chemical Society 128 (2006) 8722–8723.

[26] D. Sakellariou, G. Le Goff, J.F. Jacquinot, High-resolution, high-sensitivity NMR of nanolitre anisotropic samples by coil spinning, Nature 447 (2007) 694–698.

[27] L.C.M. van Gorkum, J.M. Hook, M.B. Logan, J.V. Hanna, R.E. Wasylishen, Solid-state lead-207 NMR of lead(II) nitrate: localized heating effects at high magic angle spinning speeds, Magnetic Resonance in Chemistry 33 (1995) 791–795.

[28] A. Bielecki, D.P. Burum, Temperature dependence of ^{207}Pb MAS spectra of solid lead nitrate. An accurate, sensitive thermometer for variable-temperature MAS, Journal of Magnetic Resonance Series A 116 (1995) 215–220.

[29] G. Vanmoorsel, E.R.H. Vaneck, C.P. Grey, $Pr_2Sn_2O_7$ and $Sm_2Sn_2O_7$ as high-temperature shift thermometers in variable-temperature Sn-119 Mas NMR, Journal of Magnetic Resonance Series A 113 (1995) 159–163.

[30] C.P. Grey, A.K. Cheetham, C.M. Dobson, Temperature-dependent solid-state Sn-119 MAS NMR of $Nd_2Sn_2O_7$, $Sm_2Sn_2O_7$, and $Y_{1.8}Sm_{0.2}Sn_2O_7$—3 sensitive chemical-shift thermometers, Journal of Magnetic Resonance Series A 101 (1993) 299–306.

[31] J.A. Stringer, C.E. Bronnimann, C.G. Mullen, D.H.H. Zhou, S.A. Stellfox, Y. Li, E.H. Williams, C.M. Rienstra, Reduction of RF-induced sample heating with a scroll coil resonator structure for solid-state NMR probes, Journal of Magnetic Resonance 173 (2005) 40–48.

[32] C.V. Grant, S.L. Sit, A.A. De Angelis, K.S. Khuong, C.H. Wu, L.A. Plesniak, S.J. Opella, An efficient H-1/P-31 double-resonance solid-state NMR probe that utilizes a scroll coil, Journal of Magnetic Resonance 188 (2007) 279–284.

[33] P.L. Gor'kov, R. Witter, E.Y. Chekmenev, F. Nozirov, R. Fu, W.W. Brey, Low-E probe for F-19-H-1 NMR of dilute biological solids, Journal of Magnetic Resonance 189 (2007) 182–189.

[34] L.D. Landau, E.M. Lifshitz, L.P. Pitaevskii, Electrodynamics of Continuous Media, Pergamon Press, Oxford, 1960.

[35] A.D. Abramov, Eddy current losses in rotating magnet fields, Russian Physical Journal (1971) 38–41.

[36] J. Lameraner, M. Stafl, Eddy Currents, Illife Books, London, 1966.

[37] W.R. Smythe, Static and Dynamic Electricity, McGraw Hill, New York, 1968.

[38] G. Meunier, J.C. Sabonnadiere, J.L. Coulomb, The finite element post-processor of FLUX3D (field computation package), IEEE Transactions on Magnetics 27 (1991) 3786.

[39] L.C.M. van Gorkom, J.M. Hook, M.B. Logan, J.V. Hanna, R.E. Wasylishen, L.C.M. van Gorkom, J.M. Hook, M.B. Logan, J.V. Hanna, R.E. Wasylishen, Solid-state lead-207 NMR of lead (II) nitrate: localized heating effects at high magic angle spinning speeds, Magnetic Resonance in Chemistry 33 (1995) 791–795.

[40] O. Dmitrenko, S. Bai, P.A. Beckmann, S. vanBramer, A.J. Vega, C. Dybowski, The relationship between ^{207}Pb NMR chemical shift and solid-state structure in Pb(II) compounds, The Journal of Physical Chemistry. A 112 (2008) 3046–3052.

[41] T. Mildner, H. Ernst, D. Freude, ^{207}Pb NMR detection of spinning-induced temperature gradients in MAS rotors, Solid State Nuclear Magnetic Resonance 5 (1995) 269.

[42] V. Malba, R. Maxwell, L.B. Evans, A.E. Bernhardt, M. Cosman, K. Yan, Laser-lathe lithography—a novel method for manufacturing nuclear magnetic resonance microcoils, Biomedical Microdevices 5 (2003) 21–27.

[43] H. Mekaru, S. Kusumi, N. Sato, M. Shimizu, M. Yamashita, O. Shimada, T. Hattori, Fabrication of a spiral microcoil using a 3D-LIGA process, Springer, 2007. pp. 393–402.